



Deposited via The University of Sheffield.

White Rose Research Online URL for this paper:

<https://eprints.whiterose.ac.uk/id/eprint/196604/>

Version: Published Version

---

**Article:**

Arce, A., Le Galliard, C., Komkova, A. et al. (2023) Optimal design of ferronickel slag alkali-activated mortar for repair exposed to high thermal load. *Materials and Structures*, 56 (2). 34. ISSN: 1359-5997

<https://doi.org/10.1617/s11527-023-02117-9>

---

**Reuse**

This article is distributed under the terms of the Creative Commons Attribution (CC BY) licence. This licence allows you to distribute, remix, tweak, and build upon the work, even commercially, as long as you credit the authors for the original work. More information and the full terms of the licence here:

<https://creativecommons.org/licenses/>

**Takedown**

If you consider content in White Rose Research Online to be in breach of UK law, please notify us by emailing [eprints@whiterose.ac.uk](mailto:eprints@whiterose.ac.uk) including the URL of the record and the reason for the withdrawal request.



# Optimal design of ferronickel slag alkali-activated mortar for repair exposed to high thermal load

Andres Arce · Cassandre Le Galliard · Anastasija Komkova · Catherine G. Papanicolaou · Thanasis C. Triantafillou

Received: 13 September 2022 / Accepted: 23 January 2023  
© The Author(s) 2023

**Abstract** In this work, the optimal design of a mortar based on alkali-activated material technology is presented. Ferronickel slag, a byproduct of the ferronickel alloy industry, was used both as a binder component (in a finely ground form) and as fine aggregate in alignment with a circular economy approach. The proportions of binder, fine aggregate, and water were optimized using Design of Experiment Design of Mixtures. The performance indicators evaluated were flow, flexural and compressive strength both before and after high-temperature exposure, mass loss, and thermal shrinkage. Life cycle assessment was used to calculate the relative environmental cost of the studied mixes in comparison to a counterpart traditional Ordinary Portland Cement mortar. The optimal mix design exhibited high flexural strength (8.5 and 10.5 MPa, before and after high-temperature exposure, respectively), an unheated compressive strength equal to 69.5 MPa, and a post-

heating residual one of 33.9 MPa, 7.7% mass loss and 3.4% thermal shrinkage. Mercury Intrusion Porosimetry along with Scanning Electron Microscopy with Energy Dispersive X-Ray Analysis were also performed on optimal mortar samples in order to link micro-structural heat-induced changes to residual (post-heating) macro-mechanical performances. Finally, when compared to OPC-based products, the optimized mortar mix resulted in 70% lower CO<sub>2</sub> emissions indicating great potential for the construction sector where concern about environmental impact keeps growing.

**Keywords** Alkali-activated cement · Mortar · Refractory cement · Waste management · Modeling

## 1 Introduction

The globe is currently facing a climate change crisis, which needs to be addressed in all sectors including the construction industry. This sector produces approximately 1.28 billion of CO<sub>2</sub> every year [1], as a direct result of the production of 1.6 billion tons of Ordinary Portland Cement (OPC). While a lot of attention has been given to the reduction in CO<sub>2</sub> emissions produced by the transportation sector, the cement industry alone is responsible for 5–8% of total global emissions [2]. An alkali-activated material (AAM) is produced by activating an aluminosilicate

---

A. Arce (✉) · C. G. Papanicolaou · T. C. Triantafillou  
Department of Civil Engineering, University of Patras,  
26504 Patras, Greece  
e-mail: andres@upatras.gr

C. Le Galliard  
Department of Materials Science and Engineering,  
University of Sheffield, Sir Robert Hadfield Building,  
Mappin Street, Sheffield S1 3JD, UK

A. Komkova  
Department of Civil, Environmental and Geomatic  
Engineering, ETH Zurich, 8093 Zurich, Switzerland



source (precursor) with an alkaline solution (activator). AAM technology has been reported to reduce CO<sub>2</sub> emissions by as much as 80% [3] when compared to OPC; therefore, it represents a potential tool to reduce CO<sub>2</sub> emissions in the construction industry. Additionally, AAM prepared with low calcium aluminosilicate sources is known for its great durability against high temperatures and chemical attacks [4]. The main goal of the work presented herein is the exploitation of this favorable AAM feature, to produce a high temperature-resistant mortar with a strong emphasis on simultaneously reducing greenhouse emissions. An additional benefit is the replacement of natural resources with existing and unexploited industrial byproducts which simultaneously addresses the problem of natural resources depletion and the logistics of byproducts storage.

OPC-based mortars conserve little to none of their strength after exposure to a high thermal load. Zhang et al. reported only 10% residual compressive strength after exposing an OPC-based mortar to a thermal load of 800 °C for 1 h [5]. The strength degradation comes from the increased chemical instability of the OPC matrix as the temperature increases. Chemical bonds' and compounds' deterioration occur at temperatures ranging between 330 and 400 °C. As the temperature increases the matrix progressively degrades. Calcium carbonate—a fundamental component of Portland cement—decomposes at 700 °C and melts at 800 °C [6]. Low-calcium AAM mortars, on the other hand, can maintain their initial strength or even show an increase [7] in residual strength after high-temperature exposure. A similar phenomenon was observed in this study where ferronickel slag (FNS)-based AAM showed higher residual flexural strength after exposure to a thermal load of 900 °C for 2 h.

Ferronickel slag is a byproduct of the ferronickel industry. In Greece alone, around 2 million tons of ferronickel slag are produced every year [8]. Only up to 30% of this amount is being reused in the cement industry and as a sandblasting material in the construction sector; the rest ends up being disposed of in landfills or under the sea [9]. Disposal cost for the unutilized slag reached 650,000 €/year in 2007 [9]. An increase in the reuse of this slag for mortar development not only would cut CO<sub>2</sub> emissions in the construction sector but would aid the metal industry to become more sustainable by reducing the problems associated with the allocation. Worldwide, millions of

tons of metallic slags (not only ferronickel) are disposed of on/underground resulting in enormous environmental impacts [9, 10]. In this paper, the authors aim to maximize the utilization of ferronickel slag not only in the binder composition as ground ferronickel slag (GFNS) but also as a fine aggregate. Previous works had shared the same objective and aimed to introduce back into the economy stainless steel slags in cement and mortars [11], steel slags in road pavements [12], and ferronickel slag in fire protection systems [13].

This study has focused its attention on ferronickel slag due to its large availability in Greece, and its proven application in the development of fire-enduring materials (see Sakkas et al. [13]). Sakkas' work proved it possible to develop a variety of construction products with GFNS ranging from high-strength cementitious binders (as high as 120 MPa) to low-strength fire-retardant coatings with a thermal conductivity as low as 0.27 W/mK. A previous study led by the first author of the present work resulted in the formulation of a binder specifically suited for high-temperature applications [14]. In the present work, this binder made of GFNS, silica fume (SF), potassium hydroxide (KOH), and potassium silicate (KS) was mixed with water and coarse FNS (sieved below 2 mm for use as fine aggregate) to develop a mortar durable under high temperature exposure. In order to optimize constituent materials' proportions with respect to a set of predetermined properties, the authors (as in the case of the binder) implemented a statistical tool, namely Design of Experiment (DOE) and—specifically—Design of Mixtures. The performance of each mix was measured using flow along with mass loss, thermal shrinkage, and residual strength after high-temperature exposure as indicators. DOE has been widely accepted in the chemical, food, and pharmaceutical industries; only recently did material scientists take advantage of this technique in the concrete industry [15]. A study by Komnitsas et al. [9] relied on another type of DOE (factorial design) for the optimization of a ferronickel slag binder with an emphasis on the factors that affect strength such as the age of testing, curing temperature, and curing time.

The result of the mix design study presented herein is an optimal mortar formulation with relatively high (compared to values from literature) flexural and compressive strength both before and after high-temperature exposure, and low mass loss, yet with a



higher-than-expected thermal shrinkage. The mortar may be used as a heat-resistant matrix for both inorganic-based composites and structural concretes. As for the first application, the optimized mortar can be combined with textiles (non-metallic fibrous grids) to be used in strengthening works as an externally bonded textile reinforced mortar (TRM) overlay. Based on the author's experience, such mortar would be required to have a minimum of 6 MPa of flexural strength and adequate consistency to allow blocking-free flow through textile openings. Through visual observations, this capacity calls for a minimum of 180 mm of flow (albeit more fresh-state evaluation tests are needed to efficiently characterize the flowability/penetrability of the mortar). All samples were prepared at ambient temperature (without heat curing) to consider the need for easy and low-energy on-site application.

## 2 Materials and methods

### 2.1 Materials

The primary aluminosilicate source material used in preparing the mortar was FNS. The slag was kindly provided by The General Mining and Metallurgical Company SA in Greece, better known as LARCO, Larissa, Greece. Micro-silica with at least 85% SiO<sub>2</sub> content was used. The particle size distribution of both ingredients was obtained through laser diffraction using a Malvern Mastersizer 2000. The d<sub>50</sub> and d<sub>90</sub> values of GFNS were 8.36 and 29.1 μm, respectively. The same indicators were, respectively, found to be 12.87 and 29.98 μm for SF.

KS and KOH were used as chemical activators. KS in the form of an aqueous solution of modulus 1.6 called Geosil® 14,517 (45% dry content) was selected. Pellets of KOH of 90% purity were used. Potassium instead of the more popularly studied sodium activators were preferred as they have been reported to yield higher residual strength after high-temperature exposure [16]. A simple example was provided by Kovalchuk and Krivenko [17] by comparing two mineral phases: orthoclase (K<sub>2</sub>O·Al<sub>2</sub>O<sub>3</sub>·6SiO<sub>2</sub>) and albite (Na<sub>2</sub>O·Al<sub>2</sub>O<sub>3</sub>·6SiO<sub>2</sub>); the fusion temperature of the former is by 52 °C higher than the one of the latter due to the replacement of a sodium atom with a potassium one. During the screening

phase for constituent materials, the effect of superplasticizers (SP) on the performance indices was also accounted for. Polycarboxylate-based SPs (MasterGlenium 347, SKY 645, and ACE345) were considered along with two naphthalene-based (Reotol-SPL and Master Rheobuild 1000) and a ligno-sulphonate-based one (MasterPozzolith 390N).

Table 1 shows the chemical composition of GFNS and SF. The data was obtained via X-Ray Fluorescence (XRF) measurements of the major (SiO<sub>2</sub>, Al<sub>2</sub>O<sub>3</sub>, CaO, MgO, MnO, Fe<sub>2</sub>O<sub>3</sub>, K<sub>2</sub>O, Na<sub>2</sub>O, P<sub>2</sub>O<sub>5</sub>, TiO<sub>2</sub>) and minor elements. Wax (0.2 g as a binder) was combined with 1.8 g of ground and dried samples and was pressed on a base of boric acid to a circular pellet of 32 mm diameter. A RIGAKU ZSX PRIMUS II spectrometer was used to perform the analysis. Major and trace elements were analyzed with an Rh-anode running at 4 kW. Diffracting crystals equipped were: LIF (200), LIF (220), PET, Ge, RX-25, RX-61, RX-40, and RX-75.

The amount of dry ingredients for 1 ton of optimized GFNS-based dry binder corresponds to 846.1 kg GFNS, 62.4 kg SF, 27.2 kg KOH and 64.4 kg KS based on [14]. These proportions were kept constant in all mortar formulations. In the following, efforts were focused on finding the ratio between the optimized GFNS binder, FNS fine aggregates, and water that produces the best-performing mortar in terms of consistency, volume stability, and strength (both unheated and heated). Information regarding these three components is reported in Table 2 including data on carbon emissions, energy consumption, and component limit proportions, by weight. The CO<sub>2-eq.</sub> emissions were estimated using the SimaPro v8.5 software linked to the Ecoinvent v3.4 database.

Ferronickel slag has previously been tested for use as fine aggregate in OPC-based mortars in which higher compressive strengths were achieved by replacing natural sand with FNS [18]. The main reported concern for using FNS as aggregate is the potential alkali-silica reaction due to the high reactive silicate content in this material. This concern was debunked in a study by Thompson et al. [19] which reported that the aluminosilicate in the slag absorbed free alkali from the AAM matrix. The absorption resulted in a significant reduction of the alkali-silica reaction potential and even resulted in high-strength mortars. Another reason to use FNS as fine aggregate

**Table 1** Ferronickel slag and silica fume chemical analysis through XRF, by weight\*

Precursor	SiO <sub>2</sub> (%)	Al <sub>2</sub> O <sub>3</sub> (%)	CaO (%)	Fe <sub>2</sub> O <sub>3</sub> (%)	MgO (%)	Na <sub>2</sub> O (%)	P <sub>2</sub> O <sub>5</sub> (%)	K <sub>2</sub> O (%)	TiO <sub>2</sub> (%)	MnO (%)	LOI- Flux
Ferronickel slag	36.9	3.61	4.18	32.8	7.41	0.15	0.02	0.48	0.19	0.00	0.00
Silica fume	88.9	0.73	0.34	1.01	0.63	0.71	0.03	1.50	0.00	0.12	6.82

\*Only detectable chemical compounds are listed

**Table 2** CO<sub>2</sub>-eq., energy consumption, and DOE boundaries for GFNS mortar ingredients

Material	Component code	CO <sub>2</sub> -eq. (kg/t)	Energy consumption (MWh/t)	Mixture boundaries, by weight (%)	
				Lower bound (%)	Upper bound (%)
GFNS binder	A	127.0	0.1760	31.2	45.1
FNS sand	B	12.1	0.0447	43.9	60.4
Water	C	–	–	8.2	11.0

is the increased thermal insulation effect. Saha et al. [20] reported that the thermal conductivity of OPC mortars decreased from 2.34 to 1.65 W/mK and 1.16 W/mK as silica sand was replaced by FNS fine aggregate by 50 and 100%, respectively.

## 2.2 Experimental methods

Apart from the mixes designed, produced, and evaluated during the screening phase (see further below), 15 combinations of GFNS binder, FNS sand, and water were prepared. For each combination, 6 prisms were cast. Mortar was prepared by mixing premade alkaline solution with SF, GFNS, and FNS sand. The alkaline solution was prepared one day in advance of mortar preparation, by adding water in a plastic container followed by Geosil® 14517; KOH pellets were added last. Immediately after the addition of KOH, the container was closed and agitated for no more than 5 s; then, the cap was removed to allow for built-in pressure to be released. The procedure was repeated for around 2 min. Mortar was prepared in 5 kg batches. For each batch, the dry ingredients (GFNS, SF, and FNS sand) were weighted and dry-mixed until a homogeneous blend was achieved. The corresponding amount of chemical activator solution was then added and hand-mixed until all liquid was absorbed. The hand-mixing step was followed by

mixing in a bench-mounted electric mortar mixer for 2 min at low speed followed by 3 min at high speed. Mortar consistency was evaluated with the flow table test and expressed in terms of the mean diameter of the mortar after jolting the table 15 times (EN 1015-3). The mortar was cast in two molds to produce 6 prisms each measuring 40 × 40 × 160 mm. Molds were vibrated for 30 s on an electric shaking table. Samples were demolded after 24 h and left to cure in two airtight plastic bags (double layer of protection) to prevent moisture loss (3 prisms per double bag). The samples were left in the bags at approximately 20 ± 5 °C for 28 days; no heat curing was used to ensure future cost-effectiveness and ease of production for practical applications.

A vernier caliper was used to measure the dimensions of the prisms both before and after high-temperature exposure to determine thermal shrinkage. Likewise, the mass was recorded using an electronic scale to calculate the mass loss. From the six prisms produced for each combination of binder, fine aggregate, and water, three prisms were exposed to a thermal load of 5 °C/min up to 900 °C; the temperature was then kept constant for two hours. The samples were left to cool down in the oven with the door closed until the following day. This heating regime has previously been used in similar studies done by Carabba et al. [21], Li et al. [22], Vickers et al.



[23], An et al. [24], and Kohout et al. [25] (in the last three with slight variations). A 500 mm<sup>3</sup> electrical oven with a maximum operating temperature of 1100 °C was employed. The remaining three prisms were kept as the control samples for unheated performance evaluation.

Flexural and compressive strengths were measured according to EN 1015-11 (yet, in a displacement-controlled mode) with a loading rate set to 0.003 mm/s. The properties were measured in both the pre- and post-heated state. It is well-known that the residual compressive strength of concrete following high-temperature exposure (concrete heated under ‘unstressed’ conditions and tested under a cooled-down state) is lower than its ‘hot’ compressive strength (both under ‘unstressed’ and ‘stressed’ conditions) [26, 27]. Thus (and extrapolating from data on concrete), the residual compressive strength values reported in this study are deemed to be a conservative estimation of the compressive capacity of heated GFNS mortars.

### 2.3 Design of experiment (DOE)

Design Expert® Software v11.1.2.0 (Stat-Ease Inc., Minneapolis, MN) was selected to define numerous mortar mix designs whose responses (measurable performances) would permit the derivation of regression equations (‘models’) in an effort to express these performances (namely, flow, mass loss, thermal shrinkage, unheated and heated compressive and flexural strengths) as a function of ingredients’ proportions. The design of an experimental matrix in this software requires the definitions of mixture components (constituent materials) and probable restrictions on their proportions. The three components for mortar design, namely GFNS binder (a previously optimized combination of GFNS, SF, KOH, and KS), fine aggregate (ferronickel slag), and water were varied in 15 combinations to produce 5000 g of mortar per batch. Before deciding on the use of these components, other additional possible constituent materials (superplasticizers) were tested in a screening study. A small amount (15 ml) of water was replaced by SP (6 products tested, 1% dose by weight). The SPs did not show any evidence of an improvement in the rheology of the mortars and were removed from consideration in the DOE test matrix. Each of the three components selected was bound to range between certain proportion boundaries (see Table 2) so that

realistic mix designs could be produced delivering flowable but also cohesive mixes. Along these lines, the water-to-binder (w/b) ratio was set between 0.243 and 0.350, the sand-to-binder ratio was kept between 0.5 and 2.0 and the solid-to-liquid ratio was set between 8.0 and 11.3 (with solid standing for the sum of GFNS, SF, KOH, KS and FNS sand and liquid for water). These boundaries were chosen after many trials (not described here) which showed that mixtures beyond these limits would result in either zero, little, or even excessive flow.

The design comprised: 10 model points, four lack-of-fit points, and one replicate point summing to 15 combinations of components which are designated in Table 2 as A (GFNS binder), B (FNS sand), and C (water). Mix designs were generated using a D-optimality criterion. Each recipe was scaled to produce six mortar prisms for both flexural and compressive strength assessment: three unheated and three heated. In this way and for each mix design, Design Expert® software experimental matrix was fed with three results for each type of strength (flexural and compressive strength before and after high-temperature exposure), one flow test measurement, three mass loss, and three thermal shrinkage results. The DOE-produced mixes were used for the derivation of regression equations through the fitting of a quadratic Scheffe model. All mix designs (including the screening phase ones) are shown in Table 3 (compositions shown per m<sup>3</sup>).

### 2.4 Life cycle assessment (LCA) method

The goal of the life cycle assessment performed within this study is to evaluate the environmental impacts associated with the examined mortar mixes (those of the screening study included) and to compare the optimal mortar mix design to a representative OPC-based one. The functional unit applied in this analysis is 1 m<sup>3</sup> of mortar. Since all mortars were produced and cured at ambient temperatures, they did not require any extra energy to reach their hardened state. Therefore, only emissions associated with mix constituents’ production and pretreatment (where applicable) were included in the system boundaries. The analysis was performed using the SimaPro 8.5 software, where life cycle inventories (LCIs) for raw material production processes were obtained from the Ecoinvent v3.4 database.

**Table 3** Ferronickel slag-based alkali-activated mortar composition per m<sup>3</sup>

Phase	Name	GFNS (kg)	SF (kg)	KOH (kg)	KS (kg)	FNS Sand (kg)	Water (kg)*	Water-to-binder** ratio
Screening	CONTROL	1018.5	74.1	24.1	57.1	1170.7	215.4	0.18
	C_RH1000	1053.5	76.7	24.2	57.6	1210.9	217.2	0.18
	C_POZ390	1048.4	76.3	24.1	57.3	1205.0	216.1	0.18
	C_ACE347	1063.1	77.4	24.4	58.1	1221.9	219.1	0.18
	C_SKY645	1031.4	75.1	23.7	56.3	1185.5	212.6	0.18
	C_ACE345	1047.8	76.3	24.1	57.2	1204.4	216.0	0.18
	C_REOTOL	1048.0	76.3	24.1	57.3	1204.6	216.0	0.18
Characterization (DOE test matrix)	1	695.4	51.3	22.3	53.0	1458.3	205.1	0.25
	2	667.4	49.2	21.4	50.8	1522.3	207.6	0.26
	3	796.6	58.7	25.6	60.7	1433.3	229.1	0.24
	4	766.5	56.5	24.6	58.4	1472.5	233.1	0.26
	5	676.4	49.9	21.7	51.5	1520.1	238.2	0.30
	6	870.2	64.1	27.9	66.3	1388.3	250.1	0.24
	7	923.8	68.1	29.7	70.4	1376.5	265.6	0.24
	8	696.5	51.3	22.4	53.0	1551.9	262.1	0.32
	9	815.1	60.1	26.2	62.1	1379.8	263.0	0.27
	10	812.6	59.9	26.1	61.9	1375.5	262.1	0.27
	11	924.0	68.1	29.7	70.4	1205.2	282.6	0.26
	12	866.4	63.9	27.8	66.0	1298.9	285.1	0.28
	13	786.5	58.0	25.2	59.9	1440.6	289.9	0.31
	14	731.8	53.9	23.5	55.7	1461.1	284.1	0.33
	15	992.2	73.1	31.8	75.6	1141.0	285.3	0.24

\*Water stands for the sum of the water from silicate solutions and additional water used

\*\*Binder stands for the sum of GFNS, SF, KOH, and the dry part of KS

As ferronickel slag can be regarded both as waste material and as a byproduct of the ferronickel industry, two scenarios of emission allocation processes were examined: no allocation and by economic value. The FNS for use as a precursor undergoes some type of pretreatment, which is fine grinding. Energy consumption for grinding is approximately 60 kWh per ton of slag [28]. The environmental impacts associated with SF and KOH production were estimated using Ecoinvent data. An LCI for KS is not available in the database. Environmental impacts of KS were estimated using LCI data for sodium silicate production through a hydrothermal process, as both silicates have similar production processes. The IPCC2013 life cycle impact assessment method was selected to estimate the global warming potential (GWP) of both GFNS and OPC mortars.

## 2.5 Mercury intrusion porosimetry

Porosity was characterized before and after thermal loading by Mercury Intrusion Porosimetry (MIP) using a Micromeritics Autopore V porosimeter. Each sample (taken from the prism core) underwent solvent exchange before being tested. According to Zhang et al. [29], the most effective technique to preserve the microstructure while removing the free water is to exchange it with isopropanol. Consequently, each sample was immersed in isopropanol for one week after being crushed into 10 mm pieces. The isopropanol solution was changed regularly throughout this week. Thereafter, the samples were dried in an ambient environment and then stored under a vacuum at ambient temperature before performing the MIP measurements. Each sample weighed  $1.8 \pm 0.2$  g. The contact angle used during these tests was  $130^\circ$



[30]. The measurements were performed with a pressure reduced gradually to 50  $\mu\text{m Hg}$  and the mercury was filled with a surface tension of  $0.485 \text{ Nm}^{-1}$ . Afterward, at 60,000 psia the intrusion was measured.

## 2.6 Scanning electron microscopy

Environmental scanning electron microscopy and energy-dispersive X-ray spectroscopy (SEM–EDX) were performed to obtain scanning electron micrographs and elemental maps in an attempt to observe chemical elements and structural changes. Before sample preparation and analysis, the free water in the pore solution was replaced by isopropanol according to the solvent exchange method presented in Sects. 2.5. Each sample was embedded in epoxy resin before being polished and carbon-coated. A Hitachi benchtop ESEM TM3030 coupled with a Bruker Quantax 70 X-ray microanalysis detector was used to perform this test. One millimeter of working distance and 15 kV of acceleration voltage were applied.

## 3 Results and discussion

### 3.1 DOE models and optimal mortar mix

The first part of Table 4 contains the results of the tests run to explore the effect of superplasticizers (screening phase). As stated before, no substantial benefit was observed from any type of SP tested. All performance indicators are reported; their values correspond to the average of three measurements, except compressive strength, which is reported as the average of six values, and flow (one measurement per mix design).

Values for each performance indicator were input in Design Expert® software and diagnosed using several statistical tools such as normal plot, Cook's distance, and plots of Residual vs. Predicted values. Outliers identified as per the previous tools were removed from the calculation of the average performance indicator for each mixture. A regression equation was derived for each performance indicator. Corresponding coefficients are reported in Table 5. Actual model-coded coefficients of responses. Predicted values can be obtained by replacing variables *A*, *B*, and *C* with the amount in grams corresponding to each component (*A*: GFNS, *B*: FNS, *C*: water) and

adding the terms. Akaike and Bayesian information criteria (AIC and BIC), as well as adjusted  $R^2$  criteria, were considered in the formulation of each model. The selected criteria corresponded to the highest predicted  $R^2$  for each response.

Fit statistics of the generated models are reported in Table 6. For each model (that is for each predicted response), these include mean values, standard deviation values, coefficients of variation (C.V.),  $R^2$  values (different types thereof), and adequate precision. Predicted and adjusted  $R^2$  values were found reasonably close, with a difference smaller than 0.2, for all models. The adequate precision (a metric used to measure the signal-to-noise ratio) was found to be higher than 4 in all cases, this indicates a probability to detect the effect of a specific component in the measured responses of at least 80% (refers to the probability of differentiating the effect of a component when compared to the natural variation of a measured parameter, also known as noise) [15]. The  $R^2$  values for heated compressive and flexural strength corresponded to 0.54 and 0.68 respectively. These values are comparable to the  $R^2$  values of 0.71 and 0.69 computed by Kaya and Koksall [31] in a study of fly ash geopolymer mortar with cement replacement exposed to high temperature. As in the present study, the authors utilized response surface methodology to produce the regression models.

A multi-response algorithm was used to determine the optimal combination of ingredients to maximize flow and strength and minimize mass loss and thermal shrinkage. The algorithm calculates a holistic indicator known as “desirability coefficient” which ranges between 0 and 1. Each of the response models determined in Table 5 influenced this algorithm based on an importance factor (from 1 to 5) which was selected as 4 except for heated mechanical properties whose importance factor was set at 5. The higher importance given to heated strength properties is meant to reflect the relevance of these performance indicators in the design of a mortar fit for high-temperature applications. Finally, Design Expert® software relied on a hill-climbing numerical optimization algorithm to find local maxima on the surfaces associated with each model described in Table 5. A set of solutions that correspond to mix designs with the highest desirability values were provided (full list not provided). The solution with the highest desirability coefficient was selected and is

**Table 4** Experimentally evaluated responses of ferronickel slag-based alkali-activated mortars

Phase	Code	Flow (mm)	Mass loss (%)	Thermal shrinkage (%)	Flexural strength (MPa)	Heated flexural strength (MPa)	Compressive strength (MPa)	Heated compressive strength (MPa)
Screening	CONTROL	170	5.5	3.5	8.8	13.9	86.3	47.1
	C_RH1000	170	5.6	3.1	8.7	13.2	91.6	44.5
	C_POZ390	175	7.1	3.1	8.0	9.9	87.7	41.8
	C_ACE347	165	6.4	3.1	8.7	11.3	90.3	43.6
	C_SKY645	160	5.7	3.1	9.8	12.1	82.9	42.8
	C_ACE345	160	5.5	3.3	9.5	13.3	90.7	44.7
	C_REOTOL	165	5.4	3.5	7.9	12.0	79.7	44.5
Characterization (DOE test matrix)	1	185	7.7	3.4	8.8	8.9	66.9	28.3
	2	160	7.3	2.6	5.9	9.5	41.4	25.5
	3	120	6.7	2.7	6.8	10.8	46.5	32.3
	4	160	7.4	2.8	8.4	11.0	52.4	39.1
	5	160	7.3	3.0	4.8	10.0	55.7	33.3
	6	200	7.3	3.0	9.5	10.2	62.5	38.1
	7	160	8.2	2.9	7.2	7.2	53.6	24.6
	8	215	8.0	3.0	6.1	8.2	47.8	29.5
	9	195	8.0	3.3	8.1	8.9	62.7	28.7
	10	145	6.9	3.2	8.0	10.8	63.2	31.7
	11	235	10.2	3.3	8.9	8.6	54.2	32.9
	12	190	7.3	2.9	5.7	8.5	48.3	34.3
	13	195	8.1	3.1	7.0	9.8	55.5	34.8
	14	230	8.7	3.5	8.3	8.6	56.7	38.3
	15	235	8.3	3.1	8.6	9.3	58.3	37.7

reported in Table 7. For this combination of ingredients, the desirability coefficient found was 0.648. The proportion of ingredients for 1 m<sup>3</sup> for this mix design corresponded to 1027 kg of GFNS binder, 1269.5 kg of FNS sand, and 252.9 kg of water. The mix was reproduced in the laboratory and experimentally evaluated. The predicted and measured performances of this recipe are compared in Table 7. All predicted responses were found to be in good agreement with the measured ones (the maximum difference was 11.2% observed in heated flexural strength).

### 3.2 Micro-scale properties

#### 3.2.1 Mercury intrusion porosimetry

Figure 1a shows the cumulative open/interconnected pore volume evolution per pore size for the optimal mix before and after heat exposure. Based on

incremental pore volume data, the volume contained in pores of a given range of sizes was also calculated for each sample as a percentage of the total pore volume. As in the case of [32], the following pore size ranges were considered: < 10 nm; 10–100 nm; 100–1000 nm; and > 1000 nm. A graphical representation of these results is given in Fig. 1b.

As may be deduced from Fig. 1a, the total porosity of the optimal mortar increased with heating. The total porosity of the heated sample was higher than the one of the unheated, by 24%. Figure 1b suggests that a large part of the pores in the unheated sample comprised gel pores (with a size below 10 nm, as per the classification proposed by Kumar et al. [34]). For this type of geopolymer matrix, this is also verified by [35]. Gel pores (but, also, pores smaller than 100 nm) were found to be practically non-existent in the heated sample; this is mainly manifested by the plateau in the cumulative pore volume vs. pore size



**Table 5** Actual model-coded coefficients of responses

Response	A	B	C	AB	AC	BC	ABC	AB(A-B)	AC(A-C)	BC(B-C)
Flow (mm)	- 0.292	0.0163	- 0.946	$5.5 \times 10^{-5}$	$4.26 \times 10^{-4}$	$- 5.50 \times 10^{-5}$	$2.35 \times 10^{-5}$			
Mass loss (%)	$- 5.02 \times 10^{-3}$	$- 1.20 \times 10^{-3}$	- 0.281		$7.59 \times 10^{-5}$	$6.83 \times 10^{-5}$				
Thermal expansion (%)	$- 3.42 \times 10^{-3}$	$6.39 \times 10^{-5}$	- 0.0525		$1.58 \times 10^{-5}$	$1.11 \times 10^{-5}$				
Flexural strength unheated (MPa)	- 0.725	- 0.0544	- 1.18	$3.20 \times 10^{-4}$	$1.10 \times 10^{-3}$	$5.77 \times 10^{-4}$	$- 4.59 \times 10^{-7}$	$3.75 \times 10^{-8}$		
Flexural strength heated (MPa)	- 0.047	0.0133	- 0.439	$6.95 \times 10^{-6}$	$1.46 \times 10^{-4}$	$4.8 \times 10^{-5}$	$1.96 \times 10^{-8}$			
Compressive strength unheated (MPa)	5.24	1.05	- 1796	- $2.97 \times 10^{-4}$	0.603	0.581	- $9.91 \times 10^{-5}$	$2.79 \times 10^{-8}$	$- 5.37 \times 10^{-5}$	$- 4.60 \times 10^{-5}$
Compressive strength heated (MPa)	- 10.1	- 0.305	1050	2.45	- $3.63 \times 10^{-3}$	- 0.329	$5.67 \times 10^{-5}$	$9.71 \times 10^{-8}$	$3.69 \times 10^{-5}$	$2.41 \times 10^{-5}$

curve of the heated sample in Fig. 1a and is quantified in Fig. 1b. More specifically, heating resulted in the drastic decrease of pores with a diameter less than 100 nm (from approximately 45% down to 2% of the total pore volume). Inversely, the large pores' share ( $> 1000$  nm) doubled with heating (from 42 to 84%). Pores with diameters in the range of 100–1000 nm remained unchanged in volume. The elimination of gel pores may be explained as a consequence of water migration from these areas and their subsequent collapse, resulting in the formation of microcracks and macropores [33–35].

Previous studies on AAM have confirmed an increase in porosity after heat exposure. Nevertheless, results mined from the literature should be carefully evaluated; both total porosity and pore size distribution are strongly dependent upon mix design specifics (constituent materials and proportions thereof, with a special reference to sand inclusion), production practices (e.g., pressure moulding, heat curing), age at heat exposure and heating regimes (heating rate and maximum temperature). Results from [32] indicate a heating-induced (2 h at 800 °C) increase in total porosity of approximately 50 and 100% for ambient-cured FA and FA/GGBFS mortar specimens, respectively. Similar to the present work [32], note that as temperature increases (especially in the range of 800–1000 °C), the proportion of pores with larger diameters increases, corresponding to changes in the microstructure of the material.

Microcracks resulting from gel collapse can be partially sealed by densification of the matrix. Nevertheless, this phenomenon is less likely to occur in AAM activated with potassium due to higher Al–O strength, as reported by Lahoti et al. [35]. As densification becomes harder to achieve in K-activated AAM, it is possible that for the exposure duration employed herein (2 h) the entirety of the samples' cross-section did not undergo crack sealing but only their outer regions which were exposed to higher temperatures for a longer period of time (there is a time delay between increase of temperature at the surface and the core).

### 3.2.2 Scanning electron microscopy

The backscattering electron images (BSE) show the presence of FNS as unreacted ground slag particles and as sand grains (Fig. 2). The FNS particles are flat

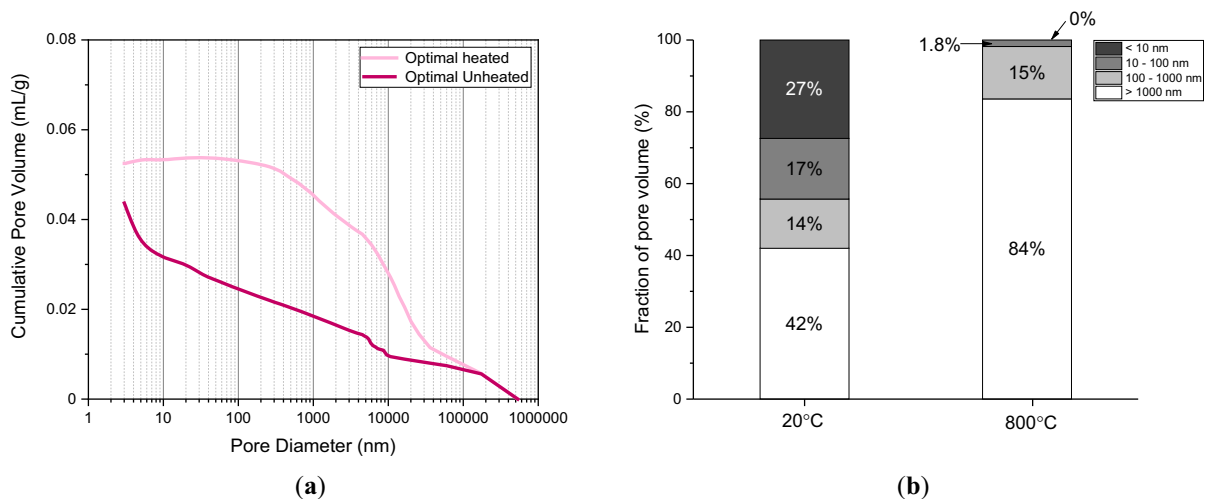


**Table 6** Fit statistics for models

Response	Mean	SD	C.V. %	$R^2$	Adjusted $R^2$	Predicted $R^2$	Adequate precision
Flow (mm)	185.57	5.59	3.01	0.97	0.97	0.97	47.7
Mass loss (%)	7.71	0.36	4.62	0.66	0.62	0.55	11.45
Thermal shrinkage (%)	-3.04	0.28	9.38	0.36	0.30	0.21	7.21
Flexural strength unheated (MPa)	7.74	0.83	10.78	0.67	0.60	0.50	8.35
Flexural strength heated (MPa)	9.36	0.74	7.85	0.68	0.63	0.56	13.28
Compressive strength unheated (MPa)	55.52	3.76	6.81	0.78	0.72	0.66	12.59
Compressive strength heated (MPa)	32.60	3.70	11.30	0.54	0.41	0.25	8.16

**Table 7** Optimized formulation and errors in predictions

	Flow (mm)	Mass loss (%)	Thermal shrinkage (%)	Flexural strength unheated (MPa)	Flexural strength heated (MPa)	Compressive strength unheated (MPa)	Compressive strength heated (MPa)
Predicted	201	7.9	3.24	8.9	9.4	64.1	34.5
Measured	185	7.7	3.35	8.5	10.5	69.5	33.9
Difference (%)	-8.0	-1.9	3.4	-5.2	11.2	7.6	-1.7

**Fig. 1** Pore size distribution before and after heat exposure: **a** Cumulative, **b** fractional share of pore size categories

with an irregular shape [36]. The darker area between the FNS particles corresponds to gel [37]. Figure 2a shows an unheated mortar section with a  $\times 40$  zoom. Micro cracks are visible, probably as a result of drying shrinkage. Figure 2b shows a heated mortar section with a  $\times 50$  zoom. Here, cracks (thermally-induced) are wider and more abundant. The cracks can be

observed not only in the matrix, but some also extend in the FNS aggregates. The widest crack in the matrix is probably a result of the tensile stress generated by the contraction of the matrix; this crack seems to have propagated into the sand particle located in the center of the image showing a strong stress transfer mechanism between matrix and aggregate. This is likely

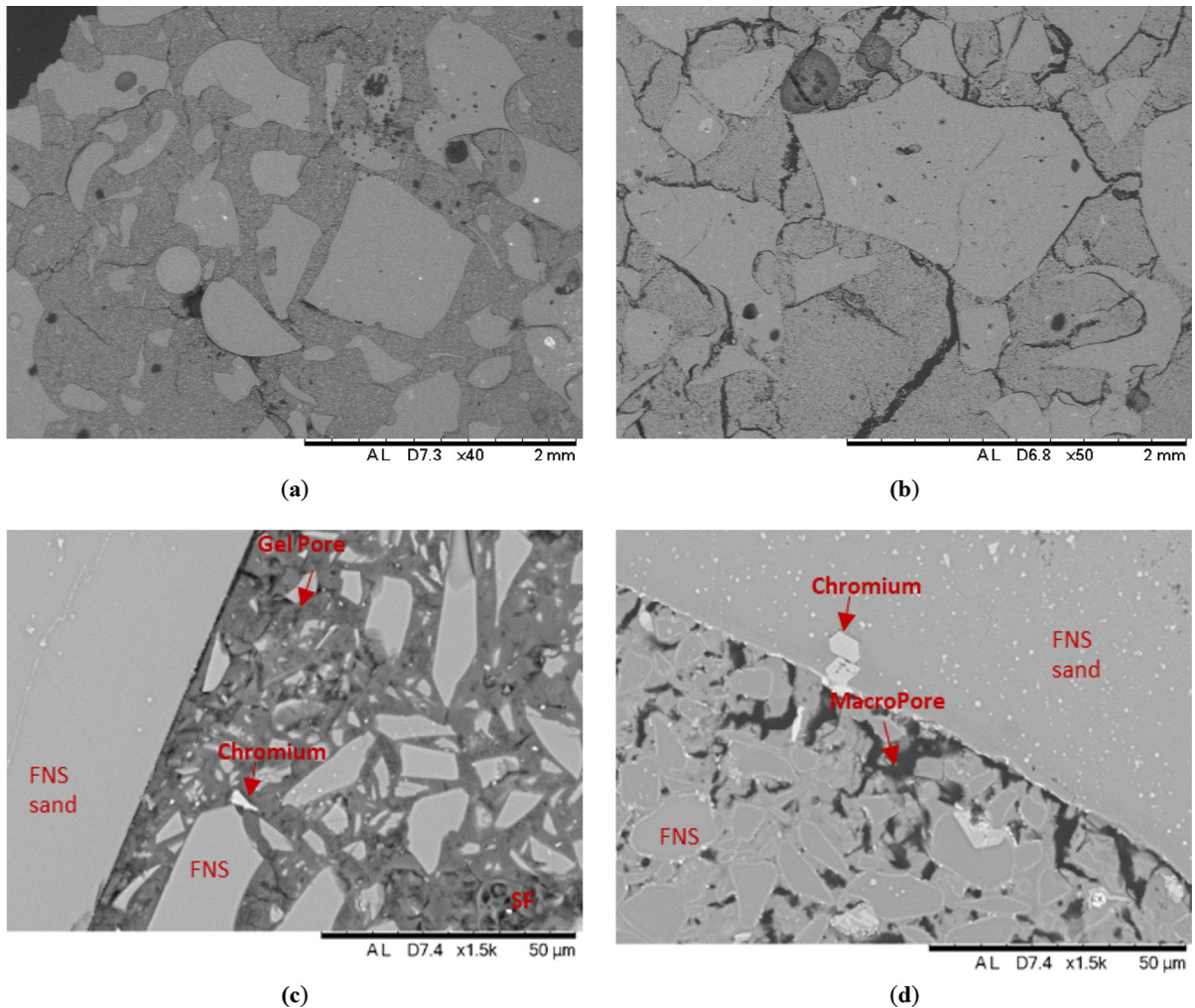


**Fig. 2** Backscattering electron images of the optimal mix: **a** unheated zoom  $\times 40$ ; **b** heated zoom  $\times 50$ ; **c** unheated zoom  $\times 1500$ ; **d** heated zoom  $\times 1500$

due to the chemical compatibility between the GFNS-based matrix and the FNS aggregate (see also the elemental map in Fig. 3 and relevant discussion further on). Figure 2c shows an unheated mortar section at a larger zoom ( $\times 1500$ ). The areas in black represent pores and cracks. At this resolution level, micro-cracks, unreacted GFNS particles, and gel pores are visible; the last two are marked in the Fig. A weak aggregate to binder bond was observed in the upper part of Fig. 2c. Analysis of other SEM images (not shown here) indicated that this is an exception and overall, there is a good bond between aggregate and binder. Figure 2d (heated mortar section at the same resolution) shows the collapse of individual gel pores and their interconnection into irregular macropores,

especially in the vicinity of the binder/aggregate transition zone with a quasi-normal orientation to the aggregate. The formation of larger pores after heat exposure is a visual confirmation of the increase in the coarseness of the pore system reported in Fig. 1. On the other hand, the observed increase of total porosity is an indication of new pores' formation (probably larger than 1000 nm) when formerly inaccessible pores (in the unheated mortar) interconnect via thermal cracking.

The elemental map of the optimal mix (Fig. 3) shows the distribution of Mg, Ca, Al, Si, K, and Cr in the mortar. These elements are present both in the FNS sand and in the GFNS except for K which was added in the form of a chemical activator and can only be

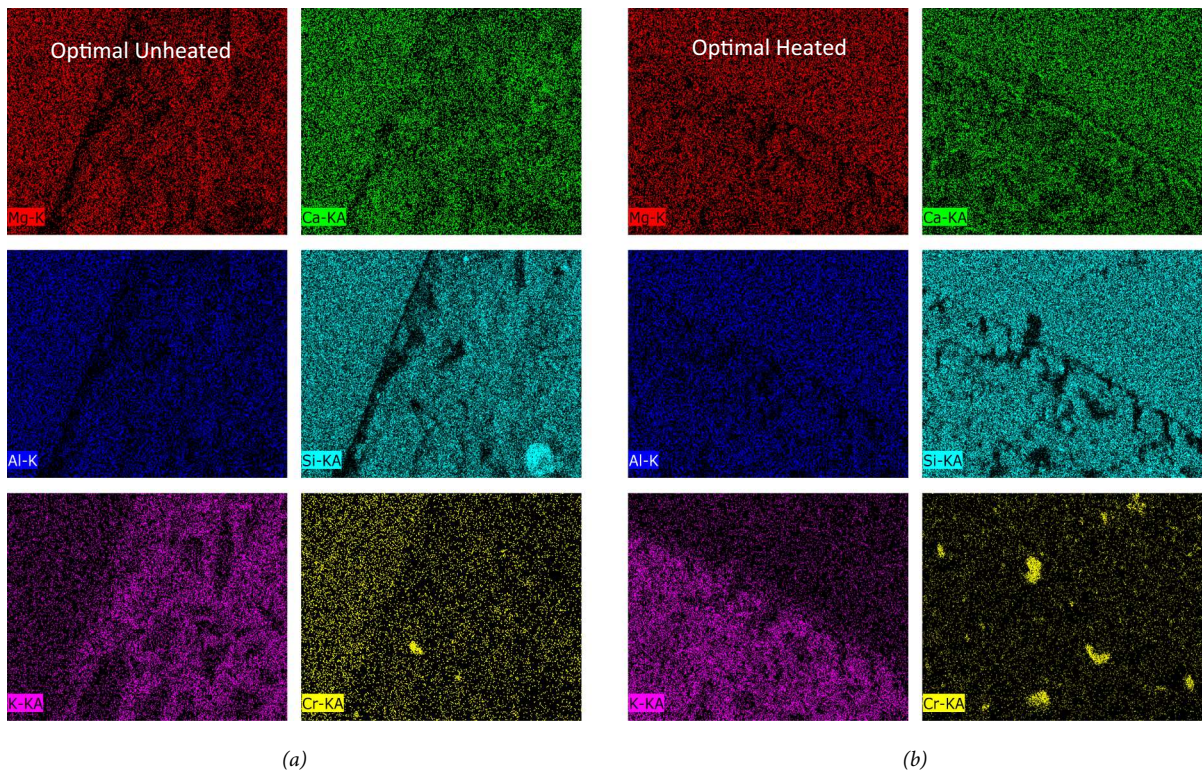


**Fig. 3** Elemental maps of the optimal mortar mix: **a** unheated; **b** heated

observed in the mortar matrix binding the sand particles together. Therefore, the K elemental map shows the frontier between FNS particles and the matrix and confirms the observations in Fig. 2. Additionally, the lack of a clear division between fine aggregate and matrix is evidence of the chemical compatibility between them as intended with the utilization of coarse (non-milled) FNS as sand. An undissolved SF particle can be observed in the silicon elemental map as a circular area in the lower right corner. Undissolved SF particles can increase the performance of AAM before and after heat exposure by acting as a micro filler.

The elemental map of this sample shows that the lighter particles in the FNS sand and the sample correspond to chromium (see also Fig. 3c, d). Cr(III) is non-toxic but the other form of Chromium such as Cr(V) and Cr(IV) present a health risk [38]. While the chromium content is of concern, previous leaching studies from Komnitsas et al. [39] have already demonstrated that once activated by an alkali metal the chromium in FNS is neutralized and exhibits zero toxicity.

### 3.3 Macro-scale properties

This section presents: (i) the flow scores of the fresh mortar samples, (ii) the visual evaluation, and (iii) the mechanical properties of the GFNS alkali-activated mortars before and after exposure to a high thermal load of 900 °C for 2 h. For the sake of comparison, the properties of other AAM and OPC mortars reported in the literature are also included. Literature-based data correspond to ambient-cured mortars subjected to a similar heating regime (800–1000 °C for a duration of 1 h to 2 h).

#### 3.3.1 Flow

Fresh mortar flow measured by the flow table test was used as an indicator of consistency. As previously mentioned, all superplasticizers studied failed to enhance the flowability of a control (reference) mortar during the screening phase. Recipes for which a small amount of water was replaced with SP resulted in less, identical, or negligibly higher flow values. The unsuitability of SPs developed for OPC-based

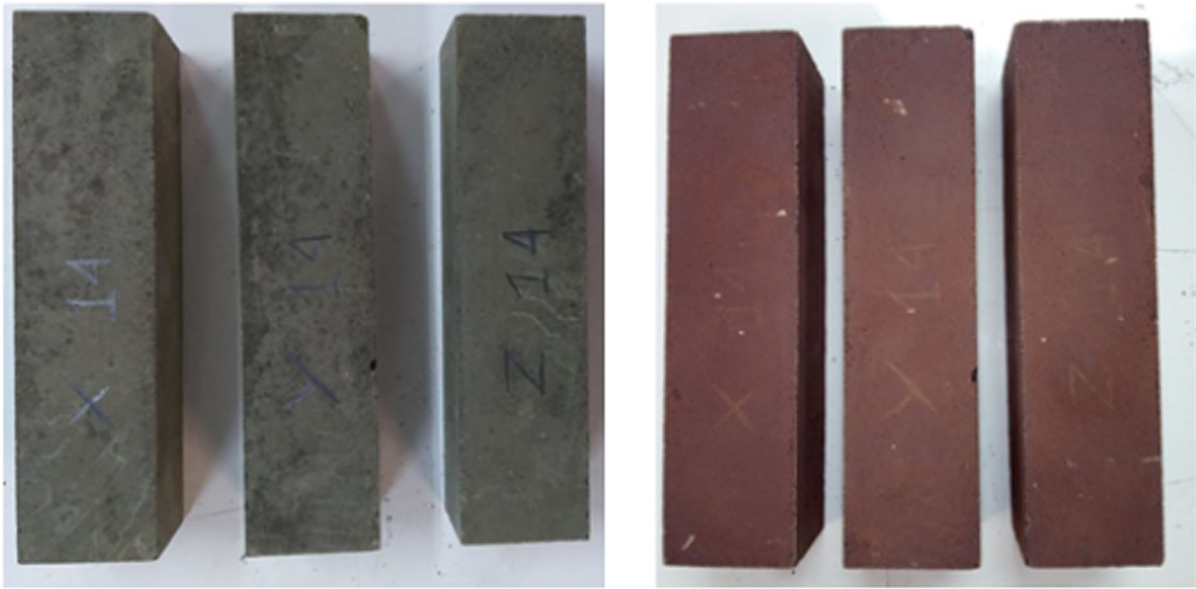


**Fig. 4** Ferronickel mortar sample (dimensions 160 mm × 40 mm × 40 mm) prior to and after high temperature exposure (left unheated, right: heated)

products for AAM ones has also been documented by other researchers (e.g. [40]). All formulations combined with a superplasticizer resulted in a decrease in flexural strength. In mix C\_POZ390 (Tables 3 and 4), a slight increase of flow was observed, accompanied by the largest drop in flexural strength (3 MPa reduction) when compared to the other SP. The lack of effect on the flow of the mortars resulted in the exclusion of SPs for the rest of the experimental campaign.

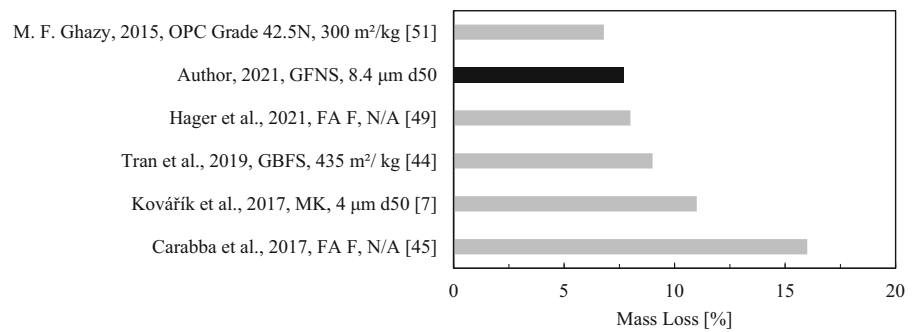
Nine out of the 15 mixes of the characterization phase passed the 180 mm flow threshold. These mixes showed a stronger dependency on the total amount of water rather than on the water-to-binder ratio. For example, mix 3 showed a much lower flow (120 mm) compared to mix 6 (200 mm) despite having the same w/b ratio (0.24). This may be a result of the loss of water due to absorption by the ferronickel aggregate (approximately 0.4% water absorption) which was 20% by weight more in mix 2. The flow of the optimal mortar mix was almost 10% lower than that predicted. Considering the poor performance of off-the-shelf SPs, they cannot be used to improve this characteristic. It might be needed to increase the w/b ratio for flow improvement depending on the application. The optimal mix was workable up to 3 h after mixing. While the workability decreased over time, it was

possible to regain some by remixing the mortar. The authors observed a strong (unquantified) dependency of workability to temperature. Trial applications on concrete surfaces (not reported here) showed a great difference in ease of application over ambient temperature variations ( $25 \pm 10$  °C) corresponding to seasonal changes in the locations where the trials were prepared (western Greece). On hot days the mix had to be modified with an extra amount of activator solution to recover the lost workability.

### 3.3.2 Appearance

Figure 4 shows typical mortar samples (the color change was almost identical for all mortars) before and after heating. The change of color from green to red is a consequence of the oxidation of iron phases present in the matrix. A similar reddish corrosion-induced coloration has been observed by Fernandez-Jimenez et al. [41], Rickard et al. [42] and Vázquez-Acosta et al. [43]. Although fine cracking is common in AAM mortars exposed to high temperatures [44], virtually no visible cracks were noticed on the prisms produced in the present study. Previous tests on GFNS alkali-activated paste run by the first author [14] showed extensive cracking. The absence of thermal cracking

**Fig. 5** Mass loss of low-calcium, ambient-cured AAM, and OPC mortars after exposure to a thermal load between 800 and 1000 °C



in mortar prisms was attributed to the crack arresting effect of fine aggregates.

### 3.3.3 Mass loss

Mass loss for all mixes generally fell within a range of 7–8%. Larger mass loss values were recorded for mixes with high water contents. There is an evident dependency between mass loss and original water content. Mix 2 had the lowest water content of all recipes and the lowest mass loss (6.7%) while mix 11 was in the upper limit of water content and evidenced a high decrease in mass (10%). Mass loss of mix 11 could also be explained by a higher percentage of large pores [45].

The water loss process was previously studied by Duxson et al. [34]. The loss of free water starts between 20 and 100 °C. Chemically bound water is then expelled between 100 and 300 °C. Finally, between 200 and 650 °C hydroxyl groups, Ca–OH, Al–OH, and Si–OH evaporate [34]. Dehydroxylation represents the second major loss of mass after free water removal [46]. The third source of mass loss is produced by the decomposition of carbonate groups [47, 48].

Mass loss of the optimal mix was either comparable or considerably lower compared to other low-calcium ambient-cured AAM mortars reported in the literature (Fig. 5). The nomenclature of each horizontal bar corresponds to the author, year of publication, precursor, and particle size indicator. ‘N/A’ stands for ‘Not Available’. The observed mass loss of the optimal mix was found to be lower than FA- [45, 49], GBFS- [44, 50], and MK- [7] based geopolymers and only slightly higher than OPC mortar [51].

### 3.3.4 Thermal shrinkage

All mortar prisms shrank by approximately 3% after heat exposure. Thermal shrinkage of AAM binders (in the range of 1–7%) has been extensively reported [5, 52, 53] and was also observed in GFNS paste prismatic specimens (7% shrinkage, as measured in a previous study led by the first author [14]). In the case of low-calcium AAM mortars assessed in the present work, thermal shrinkage was found to be much lower due to the addition of fine aggregates. A similar effect was observed by Zhang et al. [5] whose geopolymer paste thermal shrinkage was reduced from 1.1 to 0.6% as a result of river sand addition.

The thermal shrinkage of FNS-based mortars is likely a result of the geopolymer matrix contraction at high temperatures as previously reported by Rickard et al. [42] and Provis et al. [54]. These researchers found low-calcium AAM to incur a volume reduction at temperatures as low as 100 °C due to the loss of free water, followed by a secondary decrease in size due to dehydroxylation between 250 and 600 °C, with a final reduction in the range of 550–900 °C attributable to sintering of the matrix. This size reduction comes accompanied by a loss in strength which Bernal et al. [33] explained is a consequence of microcracks generated due to the partial collapse of the gel network. The collapse of the gel network as a consequence of volumetric contractions was proposed by Duxson et al. in 2007 [34]. The thermal shrinkage of the optimal mix was marginally higher than the average of all runs (3.25% compared to 3.0%). It was also higher than the thermal shrinkage of other low-calcium ambient-cured AAM mortars reported in the literature (e.g. 1.5% Kovářik et al. [7], 2% Carabba et al. [45]) and much higher than that of an OPC mortar (0.8% Cruz and Gillen [55]). It is likely that the low

thermal shrinkage values reported in the aforementioned studies are a consequence of the incorporation of fine aggregates with a high level of stability at high temperatures, such as porcelain particles used by Kovářík et al. [7] and ceramic particles used by Carabba et al. [21]. The high shrinkage of the matrix (3%) resulted in high differential thermal stresses between the fine aggregates and matrix. These stresses translated into internal damage and deterioration of mechanical properties further discussed in the following two Sects. 3.3.5 and 3.3.6.

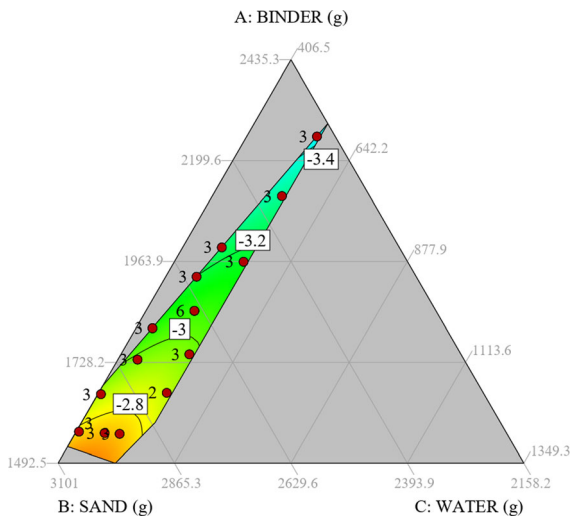


Fig. 6 2D response surface contour for thermal shrinkage

In Fig. 6, an increase in binders content in the mixture translated to higher thermal shrinkage. This behavior was previously observed by Bakharev [56] in AAM paste samples prepared with Na and K activators and exposed to temperatures between 800 and 1200 °C. While the observation refers to pure AAM paste, it is relevant to compare it to these mortar results, as even in mortar the shrinkage develops mainly as a result of the matrix shrinkage. The constraints applied to the experimental space observed in the figure resulted in a very narrow range of water variation in the mix proportions. Thus, it is difficult to come up with conclusions on the effect of water on the thermal shrinkage of GFNS mortar. The expected behavior would be an increase in shrinkage as water content increases as reported by Rickard et al. [57].

3.3.5 Flexural strength

Flexural strength values of all 15 combinations ranged between 4.8 and 9.5 MPa. Post-heating specimens exhibited either practically equal or higher flexural strengths compared to their unheated counterparts. The highest value of post-heat exposure strength corresponded to mix 4 (11 MPa), likely as a consequence of a low w/b ratio.

The 2D contour of the response surface for flexural strength (Fig. 7) allows for a visual interpretation of the effects of binder, sand, and water proportions on the mix before and after heat exposure. At ambient temperature, the highest mechanical properties can be

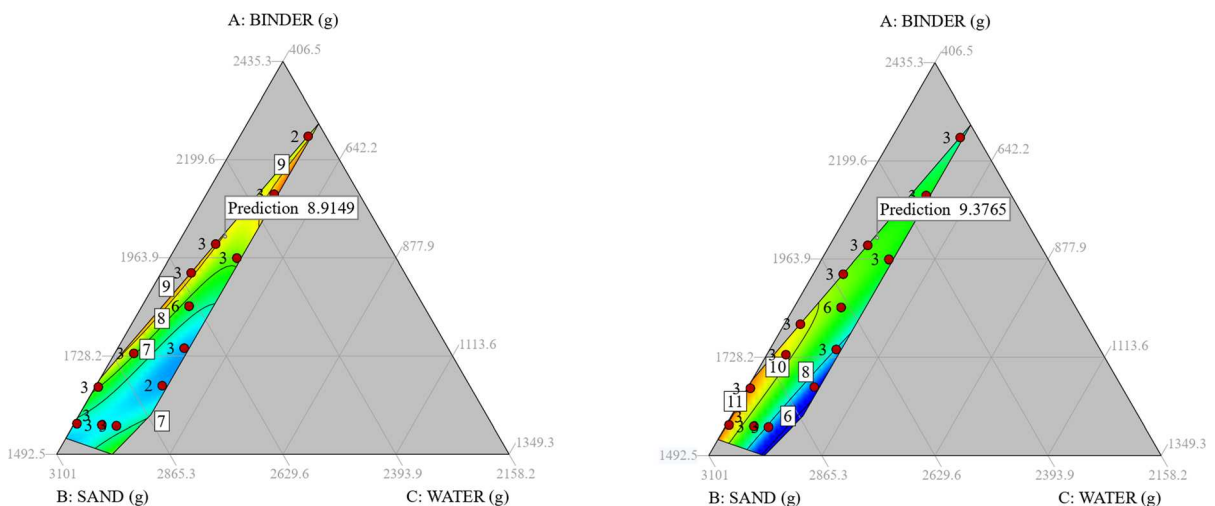
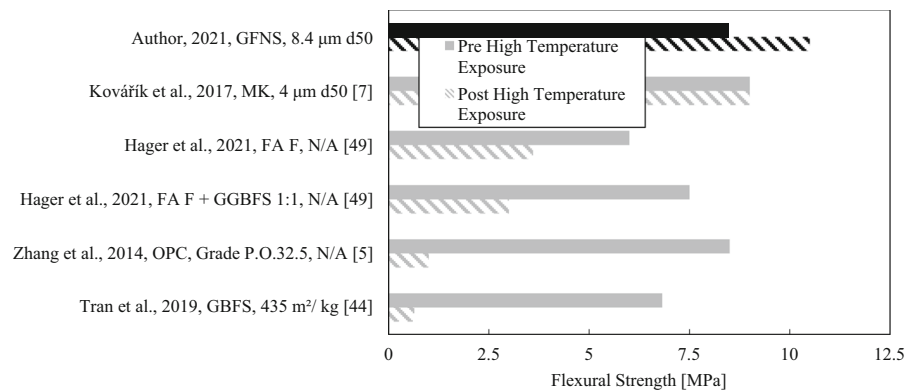


Fig. 7 2D response surface contour for flexural strength: unheated samples (left) and heated samples (right)



**Fig. 8** Flexural strength of low-calcium ambient-cured AAM and OPC mortars before and after exposure to a thermal load between 800 and 1000 °C



obtained by increasing the binder content and reducing both water and sand contents. For the high-temperature scenario, an increase of ferronickel sand would result in a higher residual flexural capacity. Regardless of temperature, the contours indicate that a lower water content promotes strength development. The optimal value marked in the Fig. 7 shows the location of the optimal point where both prior and after exposed samples have high values.

The flexural strength of the optimal mortar mix increased after exposure to a high thermal load of 900 °C and outperformed almost all other ambient-cured AAM mortars both before and after high-temperature exposure. Post-heating residual flexural strength increase has not been observed in previous relevant works where the trend is to either maintain or lose flexural strength after heat exposure. The optimal mortar mix also considerably outperformed the OPC-based mortar as reported by Zhang et al. [5]; the latter showed a decrease in residual flexural strength by almost 90%. The mix with the closest performance to the optimal one was that formulated by Kovářík et al. [7] using MK as a precursor and ceramic particles as fine aggregates. The residual flexural strength of the optimal ferronickel slag-based mortar and mortars comprising FA, GGBFS, MK, FA + GGBFS, and OPC was respectively equal to 123.5%, 60% [49], 9.4% [44], 100% [7], 40% [49] and 12% [5] of the unheated flexural strength of each mix (Fig. 8).

The increase of flexural strength with heating at 900 °C is likely a consequence of the mineral phases becoming more fluid at high temperatures and starting to densify the matrix by sealing of micro cracks [41] produced due to differential thermal stresses, and filling voids present in the material. It was expected to

observe a higher decay of flexural strength due to the high thermal shrinkage (as described in Sect. 3.3.4). It is likely that the damage was produced and the microcracks were sealed due to the sintering of the matrix, thus negating the negative effects of the micro cracks.

Normally, the coarsening of pores (see Sect. 3.2.1) would bear an adverse effect on the mechanical characteristics of the mortar including its tensile (flexural) strength. Strength increase leads to the assumption that a through-thickness differential matrix densification phenomenon took place, meaning that sintering occurred only in the outer regions of the specimen. This increased the tensile strength of the outermost tensioned fiber delaying crack formation and, hence, flexural failure of the mortar prism. It is very likely that the differential matrix densification process is associated with the duration of high temperature exposure as the outer regions reach a high temperature faster than the inner section. The delay in heating is accentuated by the decrease in thermal conductivity due to the replacement of natural sand with ferronickel slag which has been reported to be up to 50% [20].

### 3.3.6 Compressive strength

In the case of residual compressive strength gain, the trend differed from what was observed in the flexural strength test results. Residual (fractional) compressive strength values varied between 40 and 75% of the compressive strength of the unheated samples. Similar to the case of unheated flexural strength, the highest values of unheated compressive strength are found in the upper section of the ternary plot of compressive

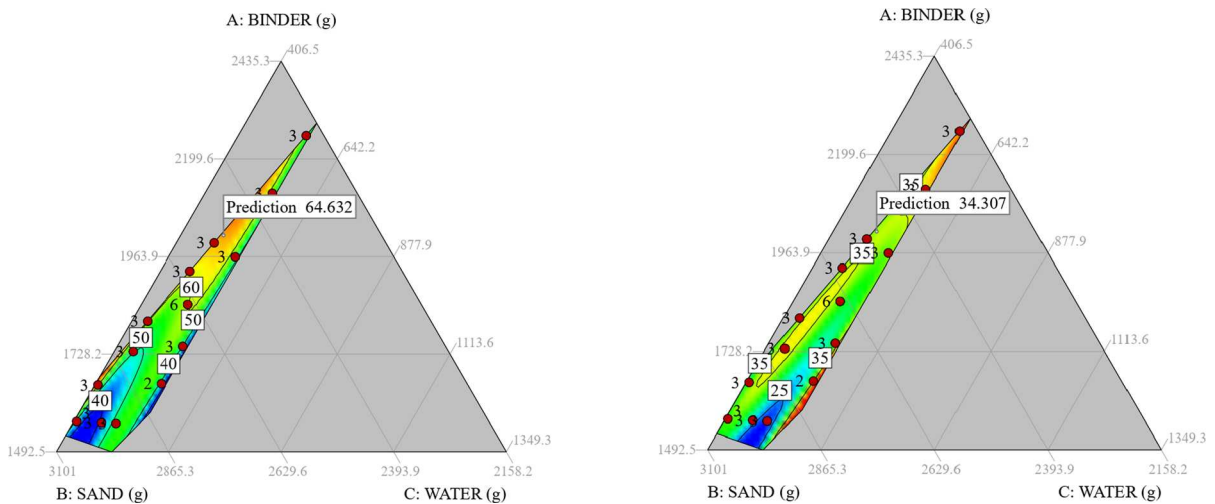
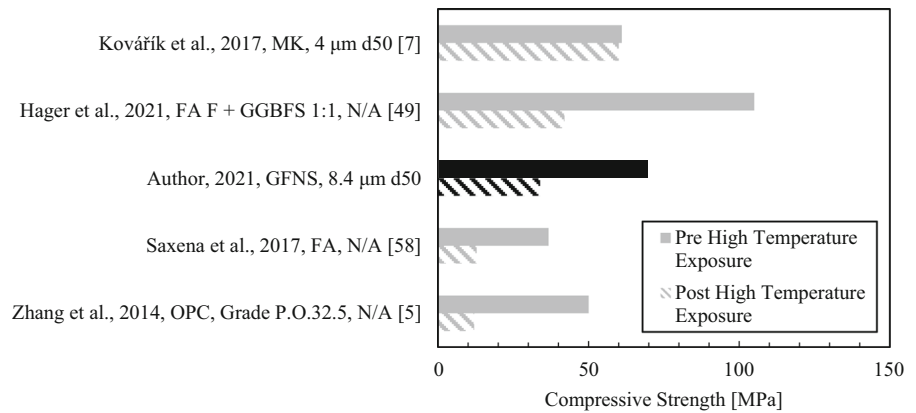


**Fig. 9** 2D response surface contour for compressive strength unheated samples (left) and heated samples (right)

**Fig. 10** Compressive strength of low-calcium ambient-cured AAM and OPC mortars before and after exposure to a thermal load between 800 and 1000 °C



strength (Fig. 9). Heated compressive strength though, showed a more complex behavior with local maxima predicted in both low and high binder content areas. This can be observed in Fig. 9b as two red color regions, one close to the maximum binder content and another one in the opposite direction and close to the peak FNS sand content.

Compared to other ambient-cured alkali-activated mortars comprising precursors from waste materials (GGFBS + FA, FA—see Fig. 10) [58], the optimum mix produced in this work exhibits superior (fractional) residual compressive strength after exposure to high temperature (amounting to approximately 50% of the unheated compressive strength). The latter is also higher than the one of the OPC-based mortar referenced in Fig. 10. The metakaolin-based mortar outperformed all others. Nevertheless, metakaolin is a

mined primary raw material that cannot be included in construction practices based on the principles of circular economy.

Strength loss has previously been explained also as a consequence of the thermal incompatibility between aggregates and binder [59–61]. FNS was chosen as fine aggregate to reduce this incompatibility since coarse slag comprises thermally stable aggregates commonly used in refractory applications, and it is also the main component (in ground form) of the binder used in this work (GFNS amounts to 84% of binder weight). Apart from the alleviation of the binder/aggregate thermal incompatibility, it is believed that binder/aggregate chemical compatibility also promotes the physicochemical interaction between the AAM gel and slag aggregates, as also suggested by [61]. Based on the above, the post-

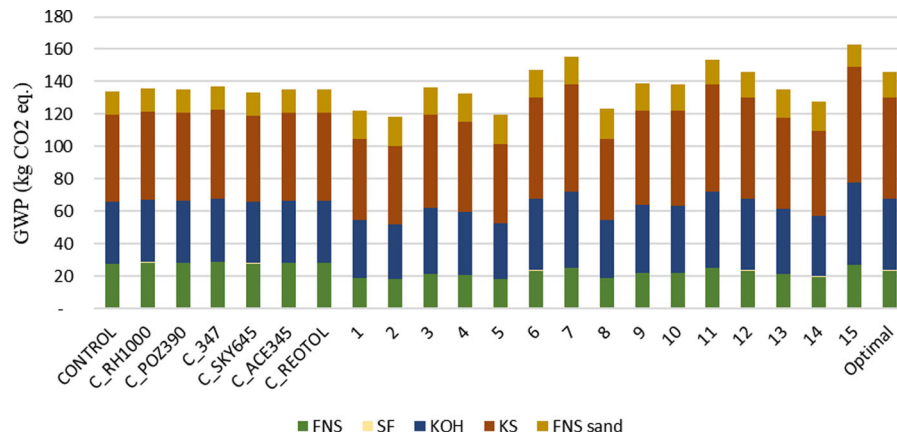


**Fig. 11** Global warming potential of FNS-based mortar mixes

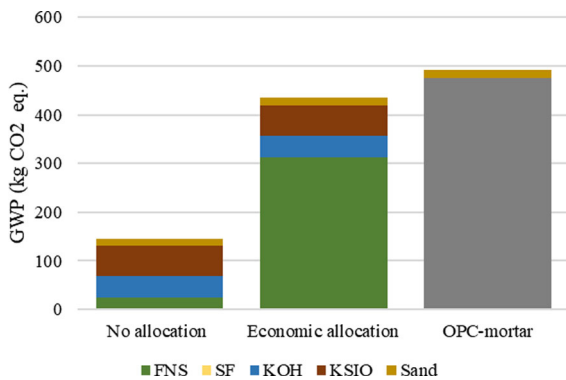


**Fig. 12** Impact of allocation method on total GWP of GFNS alkali-activated mortar compared to an OPC-based one

heating compressive strength loss observed is mainly attributed to the total porosity increase detected by MIP. Despite the densified perimeter of the prismatic pieces on which compression was exerted, the heated core was characterized by a much coarser pore structure with respect to the unheated one. This, in turn, entailed a penalty on the crushing strength of the matrix of the heated mortar.

Despite the authors efforts to reduce the thermal incompatibility of the mortar, the high thermal shrinkage (3%) resulted in differential thermal stress and damage to the matrix, thus reducing the compressive strength. In the previous section the retention of flexural strength was attributed to the sealing of micro cracks due to sintering which did not occur throughout the whole section of the samples. A localized sintering effect in the outer regions of the samples would explain why the flexural strength increased after heat

exposure and the compression strength was reduced. The flexural strength is highly influenced by the material located in the outer section, while the material in the core which is close to the neutral axis has a much lower impact on the flexural strength of the sample. The failure in compression is determined by a  $45^\circ$  plane which crossed the core of the sample. The strength is then strongly dependent of the condition of the sample core which due to a lack of sintering effect remains damaged thus reducing the measured compressive strength.

### 3.4 Life cycle analysis

All mortar recipes studied (including those in the screening study) resulted in  $\text{CO}_{2\text{eq}}$  emissions ranging from 119 to 163 kg depending on the mix design (Fig. 11). KS and KOH together contribute between 68 and 75% of the  $\text{CO}_{2\text{eq}}$  emissions to the examined impact. Here, FNS is considered a waste material. Therefore, no emissions associated with its production during the electric arc furnace smelting process were allocated; the only emissions accounted for were those associated with its grinding. Based on the above, the contribution of GFNS to the GWP was found to range between 15 and 21%. The GWP of the optimal mix design is 146 kg of  $\text{CO}_{2\text{eq}}$  emissions.

In Fig. 12, the optimal FNS mortar is compared to the OPC-based one of similar compressive strength examined by Zhang et al. [5]. Furthermore, another scenario, economic allocation, has been examined in which FNS was perceived as an industrial byproduct, instead of waste material. In the no allocation scenario,

the GWP was calculated considering the  $\text{CO}_{2\text{eq}}$  associated with SF, KOH, KSIO, sand, and the  $\text{CO}_{2\text{eq}}$  associated to the grinding process of FNS. In the economic allocation scenario, an additional  $\text{CO}_{2\text{eq}}$  referring to the production of ferronickel alloy was attributed. The percentage was calculated based on the price ratio (thus the name economic allocation) of FNS to ferronickel alloy. Hence, emissions were allocated based on economic value, namely 11.0 €/t [62] and 31 €/t (estimated to be similar to the cost of GGBFS, as reported by Hendrik G [63]) for FNS and GFNS, respectively. The ferronickel alloy value was considered as 16,000 €/t [64]. The economic allocation resulted in 434 kg  $\text{CO}_{2\text{eq}}$  per 1 m<sup>3</sup> of GFNS mortar. Following the economic allocation, the GWP of the optimal mix is 12% lower than that of the OPC-based mortar. By defining FNS as a waste material though, the respective reduction in GWP equals 70%.

#### 4 Conclusions

This study demonstrated the utility of mixture design of experiment to fine tune an alkali activated mortar recipe for high temperature conditions. The study not only found the combination of binder, fine aggregate and water to optimize the mechanical properties of the mortar, but also considered the carbon emissions and demonstrated that AAM can show similar mechanical properties to traditional mortars while resulting in much lower environmental impact. Detailed conclusions are listed below:

- DOE was proven to be a powerful tool to: (i) create a correlation between mortar performance indicators and components' proportions in the mix; (ii) help select the optimum mortar formulation that fulfills a pre-set level of combined performance desirability.
- The optimum mix design (per m<sup>3</sup>) comprised 1027 kg of GFNS binder (already optimized in [13]), 1270 kg of FNS sand, and 253 kg of water. This material may be used as a matrix for the production of heat-resistant Textile Reinforced Alkali-Activated Mortars for use mainly in the strengthening/rehabilitation of existing structures but also for prefabrication purposes.
- FNS is a suitable source for fine aggregate to develop an alkali-activated mortar suited for high-temperature applications, especially when combined with a K-activated GFNS binder. Off-the-shelf superplasticizers (designed and marketed for OPC-based products) fail to enhance the workability of such mortars.
- The post-heating (900 °C for 2 h) residual compressive and flexural strength of the optimal mix was found to be approximately 50% lower and 25% higher than the respective unheated strength values. Compared to other ambient-cured alkali-activated mortars comprising precursors from waste materials and to OPC-based mortars of similar strength class, the optimum mix produced in this work exhibits superior (fractional) residual compressive and flexural strength after exposure to high temperature.
- High mechanical properties before and after heat exposure can be obtained using this ferronickel slag fine aggregate which implies a reduction in the consumption of raw materials.
- Mass loss of the optimal mix was either comparable or considerably lower compared to other low-calcium ambient-cured AAM mortars reported in the literature and only slightly higher than that of a counterpart -strength-wise—OPC mortar. In contrast, thermal shrinkage (although manifested in a crack-free manner) was substantially higher than the aforementioned products.
- $\text{CO}_2$  savings of the optimal mortar can go as high as 70% compared to OPC-based products of similar compressive strength.

**Acknowledgements** We thank the company LARCO for the kind donation of ferronickel slag. Special acknowledgement is given to the Laboratory of Sedimentology, and the Laboratory of Electron Microscopy and Microanalysis of the University of Patras. The authors would like to acknowledge Efthymios Tasis and Yiannis Pontikes for their assistance in the processing of the FNS.

**Author contributions** AA: Conceptualization, Methodology, Software, Formal analysis, Investigation, Writing—Original Draft, Visualization AK: Methodology, Formal analysis, Writing—Original Draft CLG: Methodology, Software, Formal analysis, Writing—Original Draft, CGP: Validation, Resources, Data Curation, Writing—Review & Editing, Visualization, Supervision, Project administration, Funding acquisition TCT: Writing—Review & Editing, Visualization, Supervision, Project administration, Funding acquisition.

**Funding** Open access funding provided by HEAL-Link Greece. This research was funded by the European Union's



H2020 MARIE SKODOWSKA-CURIE ACTIONS, Grant Agreement No. 813596 DuRSAAM. The APC was funded by the University of Patras.

### Declaration

**Conflict of interest** The authors declare that they have no known competing interests.

**Open Access** This article is licensed under a Creative Commons Attribution 4.0 International License, which permits use, sharing, adaptation, distribution and reproduction in any medium or format, as long as you give appropriate credit to the original author(s) and the source, provide a link to the Creative Commons licence, and indicate if changes were made. The images or other third party material in this article are included in the article's Creative Commons licence, unless indicated otherwise in a credit line to the material. If material is not included in the article's Creative Commons licence and your intended use is not permitted by statutory regulation or exceeds the permitted use, you will need to obtain permission directly from the copyright holder. To view a copy of this licence, visit <http://creativecommons.org/licenses/by/4.0/>.

### References

- Mehta PK (2004) High-performance, high-volume fly ash concrete for sustainable development. In: International workshop on sustainable development and concrete technology, pp 3–14.
- Scrivener KL, Kirkpatrick RJ (2008) Innovation in use and research on cementitious material. *Cem Concr Res* 38(2):128–136. <https://doi.org/10.1016/j.cemconres.2007.09.025>
- Davidovits J (1994) Global warming impact on the cement and aggregates industries. *World Resour Rev* 6(2):263–278
- Shi C, Krivenko PV, Roy D (2006) Alkali-activated cements and concretes. Taylor & Francis, New York. <https://doi.org/10.4324/9780203390672>
- Zhang HY, Kodur V, Qi SL, Cao L, Wu B (2014) Development of metakaolin-fly ash based geopolymers for fire resistance applications. *Constr Build Mater* 55:38–45. <https://doi.org/10.1016/j.conbuildmat.2014.01.040>
- Li L et al (2020) A review on the recovery of fire-damaged concrete with post-fire-curing. *Constr Build Mater* 237:117564. <https://doi.org/10.1016/j.conbuildmat.2019.117564>.
- Kovářík T et al (2017) Thermomechanical properties of particle-reinforced geopolymer composite with various aggregate gradation of fine ceramic filler. *Constr Build Mater* 143:599–606. <https://doi.org/10.1016/j.conbuildmat.2017.03.134>
- Larco General Mining & Metallurgical Co., S.A., “Research and Development,” 2022. <http://www.larco.gr/rnd.php>. Accessed Sep. 21, 2022.
- Komnitsas K, Zaharaki D, Perdikatsis V (2007) Geopolymerisation of low calcium ferronickel slags. *J Mater Sci* 42(9):3073–3082. <https://doi.org/10.1007/s10853-006-0529-2>
- Mo L, Zhang F, Deng M, Jin F, Al-Tabbaa A, Wang A (2017) Accelerated carbonation and performance of concrete made with steel slag as binding materials and aggregates. *Cem Concr Compos*. <https://doi.org/10.1016/j.cemconcomp.2017.07.018>
- Rosales J, Cabrera M, Agrela F (2017) Effect of stainless steel slag waste as a replacement for cement in mortars. Mechanical and statistical study. *Constr Build Mater*. <https://doi.org/10.1016/j.conbuildmat.2017.03.082>.
- Pasetto M, Baliello A, Giacomello G, Pasquini E (2017) Sustainable solutions for road pavements: a multi-scale characterization of warm mix asphalts containing steel slags. *J Clean Prod*. <https://doi.org/10.1016/j.jclepro.2017.07.212>
- Sakkas K, Nomikos P, Sofianos A, Panias D (2014) Utilization of FeNi-Slag for the production of inorganic polymeric materials for construction or for passive fire protection. *Waste Biomass Valorization* 5(3):403–410. <https://doi.org/10.1007/s12649-013-9278-z>
- Arce A, Komkova A, Van De Sande J, Papanicolaou CG, Triantafyllou TC (2022) Optimal design of ferronickel slag alkali-activated material for high thermal load applications developed by design of experiment. *Mater* 15(13):4379. <https://doi.org/10.3390/ma15134379>
- Anderson PJ, Mark J (2007) Whitcomb, DOE Simplified, 3rd edn. CRC Press, Florida
- Komnitsas K, Zaharaki D, Perdikatsis V (2009) Effect of synthesis parameters on the compressive strength of low-calcium ferronickel slag inorganic polymers. *J Hazard Mater* 161(2–3):760–768. <https://doi.org/10.1016/j.jhazmat.2008.04.055>
- Kovalchuk G, Krivenko PV (2009) Producing fire- and heat-resistant geopolymers. *Geopolymers Struct Process Prop Ind Appl*, pp 227–266. <https://doi.org/10.1533/9781845696382.2.227>.
- Saha AK, Sarker PK (2017) Compressive strength of mortar containing ferronickel slag as replacement of natural sand. *Procedia Eng* 171:689–694. <https://doi.org/10.1016/j.proeng.2017.01.410>
- Thompson A, Saha AK, Sarker PK (2019) Comparison of the alkali-silica reactions of ferronickel slag aggregate in fly ash geopolymer and cement mortars. *Eur J Environ Civ Eng*, pp 1–14. <https://doi.org/10.1080/19648189.2019.1686068>.
- Saha AK, Sarker PK, Golovanevskiy V (2019) Thermal properties and residual strength after high temperature exposure of cement mortar using ferronickel slag aggregate. *Constr Build Mater* 199:601–612. <https://doi.org/10.1016/j.conbuildmat.2018.12.068>
- Carabba L, Manzi S, Rambaldi E, Ridolfi G, Bignozzi MC (2017) High-temperature behaviour of alkali-activated composites based on fly ash and recycled refractory particles. *J Ceram Sci Technol* 8(3):377–387. <https://doi.org/10.4416/JCST2017-00047>
- Li OH, Yun-Ming L, Cheng-Yong H, Bayuaji R, Abdullah MMAB, Loong FK, Sing NY (2021) Evaluation of the effect of silica fume on amorphous fly ash geopolymers exposed to elevated temperature. *Magnetochemistry* 7(1):9. <https://doi.org/10.3390/magnetochemistry7010009>
- Vickers L, Rickard WDA, Van Riessen A (2014) Strategies to control the high temperature shrinkage of fly ash based



- geopolymers. *Thermochim Acta* 580:20–27. <https://doi.org/10.1016/j.tca.2014.01.020>
24. An EM, Cho YH, Chon CM, Lee DG, Lee S (2015) Synthesizing and assessing fire-resistant geopolymer from rejected fly ash. *J Korean Ceram Soc* 52(4):253–263. <https://doi.org/10.4191/kcers.2015.52.4.253>
  25. Kohout J, Koutník P, Hájková P, Kohoutová E, Soukup A (2021) Effect of K/Al molar ratio on the thermo-mechanical properties of metakaolinite-based geopolymer composites. *polym* 13(21):3754. <https://doi.org/10.3390/polym13213754>
  26. Phan L (1996) Fire performance of high-strength concrete: a report of the state-of-the-art. *Fire Res.*
  27. Abrams MS (1971) Compressive strength of concrete at temperatures to 1600F. In: American Concrete Institute, ACI Special Publication.
  28. de Bakker J (2014) Energy use of fine grinding in mineral processing. *Metall Mater Trans E* 1(1):8–19. <https://doi.org/10.1007/s40553-013-0001-6>
  29. Zhang J, Scherer GW (2011) Comparison of methods for arresting hydration of cement. *Cem Concr Res* 41(10):1024–1036. <https://doi.org/10.1016/j.cemconres.2011.06.003>
  30. Zeng Q, Li K, Fen-Chong T, Dangla P (2012) Analysis of pore structure, contact angle and pore entrapment of blended cement pastes from mercury porosimetry data. *Cem Concr Compos* 34(9):1053–1060. <https://doi.org/10.1016/j.cemconcomp.2012.06.005>
  31. Kaya M, Köksal F (2021) Effect of cement additive on physical and mechanical properties of high calcium fly ash geopolymer mortars. *Struct Concr* 22(S1):E452–E465. <https://doi.org/10.1002/suco.202000235>
  32. Dudek M, Sitarz M (2020) Analysis of changes in the microstructure of geopolymer mortar after exposure to high temperatures. *Materials* 13(19). <https://doi.org/10.3390/MA13194263>.
  33. Bernal SA, Rodríguez ED, Mejía De Gutiérrez R, Gordillo M, Provis JL (2011) Mechanical and thermal characterisation of geopolymers based on silicate-activated metakaolin/slag blends. *J Mater Sci* 46(16):5477–5486. <https://doi.org/10.1007/s10853-011-5490-z>
  34. Duxson P, Lukey GC, Van Deventer JSJ (2007) Physical evolution of Na-geopolymer derived from metakaolin up to 1000 °C. *J Mater Sci* 42(9):3044–3054. <https://doi.org/10.1007/s10853-006-0535-4>
  35. Lahoti M, Wong KK, Tan KH, Yang E (2018) Effect of alkali cation type on strength endurance of fly ash geopolymers subject to high temperature exposure. *Mater Des* 154:8–19. <https://doi.org/10.1016/j.matdes.2018.05.023>
  36. Petrakis E, Karmali V, Bartzas G, Komnitsas K (2019) Grinding kinetics of slag and effect of final particle size on the compressive strength of alkali activated materials. *Minerals* 9(11). <https://doi.org/10.3390/min9110714>.
  37. Maragkos I, Giannopoulou IP, Papias D (2009) Synthesis of ferronickel slag-based geopolymers. *Miner Eng* 22(2):196–203. <https://doi.org/10.1016/j.mineng.2008.07.003>
  38. Desmaris TL, Costa M (2019) Toxicology mechanisms of chromium-induced toxicity. *Curr Opin Toxicol* 14(III):1–7. <https://doi.org/10.1016/j.cotox.2019.05.003>.
  39. Komnitsas K, Zaharaki D, Bartzas G (2013) Effect of sulphate and nitrate anions on heavy metal immobilisation in ferronickel slag geopolymers. *Appl Clay Sci.* <https://doi.org/10.1016/j.clay.2012.09.018>
  40. Kong DLY, Sanjayan JG (2010) Effect of elevated temperatures on geopolymer paste, mortar and concrete. *Cem Concr Res* 40(2):334–339. <https://doi.org/10.1016/j.cemconres.2009.10.017>
  41. Fernández-Jiménez A, Pastor JY, Martín A, Palomo A (2010) High-temperature resistance in alkali-activated cement. *J Am Ceram Soc* 93(10):3411–3417. <https://doi.org/10.1111/j.1551-2916.2010.03887.x>
  42. Rickard WDA, Van Riessen A, Walls P (2010) Thermal character of geopolymers synthesized from class F Fly ash containing high concentrations of iron and  $\alpha$ -quartz. *Int J Appl Ceram Technol* 7(1):81–88. <https://doi.org/10.1111/j.1744-7402.2008.02328.x>
  43. Vázquez-Acosta F, Torres-Martínez LM, López-González W, Ibarra-Rodríguez J (2012) Influence of iron content on the color of the C 3A-Fe 2O 3 system synthesized under different conditions of temperature, atmosphere and cooling. *Ceram Int.* <https://doi.org/10.1016/j.ceramint.2011.12.032>
  44. Tran TT, Kang H, Kwon HM (2019) Effect of heat curing method on the mechanical strength of alkali-activated slag mortar after high-temperature exposure. *Materials* 12(11). <https://doi.org/10.3390/ma12111789>.
  45. Carabba L, Manzi S, Rambaldi E, Ridolfi G, Bignozzi MC (2017) High-temperature behaviour of alkali-activated composites based on fly ash and recycled refractory particles. *J Ceram Sci Technol* 388:377–388. <https://doi.org/10.4416/JCST2017-00047>.
  46. He R, Dai N, Wang Z (2020) Thermal and mechanical properties of geopolymers exposed to high temperature: a literature review. *Adv Civ Eng.* <https://doi.org/10.1155/2020/7532703>.
  47. Rakhimova NR et al (2018) Marl-based geopolymers incorporated with limestone: a feasibility study. *J Non-Cryst Solids* 492(February):1–10. <https://doi.org/10.1016/j.jnoncrysol.2018.04.015>
  48. Nath SK, Kumar S (2020) Role of particle fineness on engineering properties and microstructure of fly ash derived geopolymer. *Constr Build Mater* 233:117294–117294. <https://doi.org/10.1016/j.conbuildmat.2019.117294>
  49. Hager I, Sitarz M, Mróz K (2021) Fly-ash based geopolymer mortar for high-temperature application—effect of slag addition. *J Clean Prod.* 316. <https://doi.org/10.1016/j.jclepro.2021.128168>.
  50. Kaya M, Köksal F (2021) Influences of high temperature on mechanical properties of fly ash based geopolymer mortars reinforced with PVA fiber. *Rev Constr* 20(2):393–406. <https://doi.org/10.7764/rdlc.20.2.393>
  51. Ghazy MF, Elaty MAA, Elkhoriy RS (2015) Performance of blended cement mortars incorporating nano-metakaolin particles at elevated temperatures. In: *Proceeding Int. Conf. Adv. Struct. Geotech. Eng. Hurghada Egypt*, pp 6–9.
  52. Rovnaník P, Šafránková K (2016) Thermal behaviour of metakaolin/fly ash geopolymers with chamotte aggregate. *Materials* 9(7). <https://doi.org/10.3390/ma9070535>.
  53. Zhang HY, Kodur V, Wu B, Cao L, Qi SL (2016) Comparative thermal and mechanical performance of



- geopolymers derived from metakaolin and fly ash. *J Mater Civ Eng* 28(2):04015092. [https://doi.org/10.1061/\(asce\)mt.1943-5533.0001359](https://doi.org/10.1061/(asce)mt.1943-5533.0001359)
54. Provis JL, Van Deventer JSJ (2009) Structures, processing, properties and industrial applications. *Geopolymers*. <https://doi.org/10.1533/9781845696382>.
55. Cruz CR, Gillen M (1980) Thermal expansion of Portland cement paste, mortar and concrete at high temperatures. *Fire Mater* 4(2):66–70. <https://doi.org/10.1002/fam.810040203>
56. Bakharev T (2006) Thermal behaviour of geopolymers prepared using class F fly ash and elevated temperature curing. *Cem Concr Res* 36(6):1134–1147. <https://doi.org/10.1016/j.cemconres.2006.03.022>
57. Rickard WDA, Williams R, Temuujin J, van Riessen A (2011) Assessing the suitability of three Australian fly ashes as an aluminosilicate source for geopolymers in high temperature applications. *Mater Sci Eng A* 528(9):3390–3397. <https://doi.org/10.1016/j.msea.2011.01.005>
58. Saxena SK, Kumar M, Singh NB (2017) Fire resistant properties of alumino silicate geopolymer cement mortars. *Mater Today Proc* 4(4):5605–5612. <https://doi.org/10.1016/j.matpr.2017.06.018>
59. Kong DLY, Sanjayan JG (2008) Damage behavior of geopolymer composites exposed to elevated temperatures. *Cem Concr Compos* 30(10):986–991. <https://doi.org/10.1016/j.cemconcomp.2008.08.001>
60. Ranjbar N, Mehrali M, Alengaram UJ, Metselaar HSC, Jumaat MZ (2014) Compressive strength and microstructural analysis of fly ash/palm oil fuel ash based geopolymer mortar under elevated temperatures. *Constr Build Mater* 65:114–121. <https://doi.org/10.1016/j.conbuildmat.2014.04.064>
61. Duxson P, Provis JL, Lukey GC, Mallicoate SW, Kriven WM, Van Deventer JSJ (2005) Understanding the relationship between geopolymer composition, microstructure and mechanical properties. *Colloids Surf Physicochem Eng Asp* 269(1–3):47–58. <https://doi.org/10.1016/j.colsurfa.2005.06.060>
62. Eramet Group (2021) Combined General Shareholders' Meeting, May 28, 2021," vol. 2020, no. May, pp. 2019–2021.
63. van Oss H (2003) Slag—iron and steel, U.S. geological survey minerals yearbook—2002, Reston, VA, USA.
64. metalshub team (2022) Metalshub—Ferronickel and nickel metal | price index. <https://www.metals-hub.com/nickel>. Accessed Dec. 20, 2022.

**Publisher's Note** Springer Nature remains neutral with regard to jurisdictional claims in published maps and institutional affiliations.

